

Pristine surface of Ni-Rich layered transition metal oxides as a premise of surface reactivity

Angelica Laurita¹, Liang Zhu², Pierre-Etienne Cabelguen², Jérémie Auvergniot², Jonathan Hamon¹, Dominique Guyomard¹, Nicolas Dupré¹, Philippe Moreau^{1,*}

¹ Nantes Université, CNRS, Institut des Matériaux de Nantes Jean Rouxel, IMN, F-44000 Nantes, France

² Umicore, 31 rue du marais, Brussels BE-1000, Belgium

KEYWORDS. lithium-ion batteries, surface reaction, Ni-rich cathode, lithium hydroxide, lithium carbonate, monochromated EELS, storage conditions, cation composition, nanometer characterization.

ABSTRACT. The surface reactivity of Ni-rich layered transition metal oxides is instrumental to the performance of batteries based on these positive electrode materials. Most often, strong surface modifications are detailed with respect to a supposed ideal initial state. Here, we study the $\text{LiNi}_{0.8}\text{Mn}_{0.1}\text{Co}_{0.1}\text{O}_2$ (NMC811) cathode material in its pristine state, hence before any contact with electrolyte or cycling, thanks to advanced microscopy and spectroscopy techniques in order to fully characterize its surface down to the nanometer scale. Scanning transmission-electron microscopy-electron energy-loss spectroscopy (STEM-EELS), solid state nuclear-magnetic-resonance (SS-NMR) and X-rays photoelectron spectroscopy (XPS) are combined and correlated

in an innovative manner. The results demonstrate that in usual storage conditions after synthesis, the extreme surface is already chemically different from the nominal values. In particular, nickel is found in a reduced state compared to the bulk value and a Mn enrichment is determined in the first few nanometers of primary particles. Further exposition to humid air allows for quantifying the formed lithiated species per gram of active material, identifying their repartition and proposing a reaction path in relation with the instability of the surface.

1. Introduction

The fast world population growth combined with life modernization due to the rapid development of new technologies have brought, over the past years, a strong increase in the demand for primary energy, which has been initially met mainly by the combustion of fossil fuels. Nowadays, to reduce the contribution of fossil resources to the existing energy mix, our modern society relies increasingly on electrochemical energy storage for the electrification of vehicles. Performance of Lithium-ion batteries, currently vastly employed for this purpose, must therefore step up as fast as the technology evolution to meet the requirements of an ever more demanding market. In a world producing more than 50 million passenger cars per year (20% of which could become hybrid electric vehicles or electric vehicles (HEV/EV) within the next 10 years), Li-ion batteries are required to provide an ever increasing energy density to guarantee a longer driving range.¹

Most positive electrode materials currently produced by the industry belong to the NMC family, layered oxides with general formula $\text{Li}(\text{Ni}_x\text{Mn}_y\text{Co}_{1-x-y})\text{O}_2$ and properties that depend on the relative amount of the different transition metals (TM).² In particular, in order to achieve a higher capacity and thence higher energy density, the research has been heading towards high Ni-content NMCs for some years now.²⁻⁵ This approach also allows lowering the Co content, reducing the

cost in the material production, its toxicity and the humanitarian issues related to Co mining.⁶ Nevertheless, by increasing the Ni content, the material thermodynamic instability increases together with the gas evolution upon electrochemical cycling, phenomenon of which the comprehension becomes an essential safety challenge at the industrial level.⁷

Many studies were conducted on Ni-rich NMCs during cycling to elucidate both the origins and the consequences of these issues. Different gases in various amounts, such as CO₂, CO and O₂, are released during electrochemical cycling as a function of the battery state of charge, the material composition and surface impurities such as Li₂CO₃.⁷⁻¹⁰ It is clear that the nature of the active material (AM) surface, which often depends on synthesis and storage conditions, leads to different reactivities towards the electrolyte. The pristine surface of the NMC material, root of later evolution during cycling, is thus of utmost importance. However, despite the large number of publications on Ni-rich NMCs, only a few studies precisely describing the pristine material can be found in the literature.^{11,12} Such a necessary understanding of the initial state of positive electrode AMs was conducted by other groups on other similar transition metal oxides such as LiCoO₂ (LCO), Li_{1.2}(Mn_{0.6}Ni_{0.2})O₂ (LMNO) and Li-Mn-rich oxides, always highlighting a different nature of the surface compared to the bulk and thence the importance of proper and thorough surface characterizations of these materials at a nanometric scale.¹³⁻¹⁶ The segregation of Co and Ni, the depletion in surface Li, together with the nucleation of domains with different structures, were observed at the surfaces of the materials in these studies.

These considerations become even more important with the development of gradient composition Ni-Rich NMCs, where surface and bulk compositions are purposely modified.¹⁷ The actual state of the surface just after synthesis needs thus to be determined precisely. Moreover, materials are usually not used straight from the furnace but are stored for a certain period before

electrode fabrication. The effect of long-term storage was investigated in various studies and correlated to the surface contamination layer evolutions and to the gassing.^{9,18–20}

Since the synthesis and storage conditions were often identified as a possible reason for the discrepancy between results obtained by different research groups, we propose to focus here on the characterization of an industrial NMC811 (UMICORE) in its initial state, as arrived from the production plant (Sample A0).^{20–22} Thanks to this approach, we provide representative results that can be generalized at an industrial level. In order to address the lack of studies on the material in its initial state previously mentioned, essential for its reactivity comprehension, we present here a complete characterization of a pristine industrial grade NMC811, down to the sub-nanometer level. We also provide a possible explanation for its behavior during storage in defined conditions.

A multi-analytical approach based on on-site characterization techniques was used to give a complete picture of this complex material at different scales. MAS-NMR was used to give a correct quantification of the Li diamagnetic species at the surface of the material, while their speciation was obtained by XPS. STEM-EDX and STEM-EELS were then used to follow the composition trend within the first nanometers of the AM surface. We present how advanced characterization techniques can be coupled and exploited in a synergetic way to detect and quantify significant surface inhomogeneities. We also show the impact of short-term low-humidity storage conditions on the formation and the distribution of new compounds at the AM surface.

2. Experimental section

2.1. Pristine samples

Pristine NMC811 powder was synthesized at Umicore company by co-precipitating sulfates of TMs in presence of NaOH followed by calcination at high temperature. The nominal composition was determined by ICP analysis, resulting to be 80.2 : 9.8 : 10.0 (Ni : Mn : Co), with a Li/Metal

ratio of 1.013. This powder was then stored in the industrial partner's dry room and shipped to us inside a sealed aluminum bag under dry atmosphere; once received, it was stored in an argon glovebox (Sample A0). The relative humidity in an industrial dry room is usually controlled to be between about 0.7 and 1.5% and could lead to some modifications of the material surface due to the extremely high reactivity of NMC811 compared to other NMCs.^{4,23}

The powder, in form of secondary particles, was manually ground in the argon-filled glovebox by using an agate mortar and a pestle, to obtain individual primary particles with a clean pristine surface (see Figure 2). Sample A0 was fully characterized and compared with Sample A1 and Sample A2 (Table 1), obtained after storage in different conditions of relative humidity (RH) and exposure time. To prepare these samples, Sample A0 was put in a climatic chamber after grinding, with controlled Relative Humidity (RH) of 30% and ambient oxygen and CO₂ partial pressures. Sample A1 was stored under these conditions for 15 minutes and sample A2 for 2 days (Table 1).

Table 1. NMC811 samples description.

Sample	A0	A1	A2
Aging conditions	Pristine	RH = 30%; t = 15 minutes	RH = 30%; t = 2 days

2.2. Electron Energy Loss Spectroscopy (EELS)

TEM Samples were deposited on a holey carbon copper grid inside the glovebox without the use of any solvent. The grid was then sealed in argon atmosphere in a vacuum transfer holder (Gatan 648). The sample surface was cleaned by means of a Fischione Instruments plasma cleaner (model 1070) with pure Ar gas for 30 seconds at a power level of 30% and a gas flow of 30 sccm. The grid was then sealed under secondary vacuum and transferred into the microscope, without the sample entering in contact with the ambient atmosphere.

STEM-EELS analyses were performed on a monochromated probe-corrected TEM/STEM Themis Z G3 (Thermo Fisher Scientific) equipped with a double camera spectrometer (Gatan Imaging Filter Quantum ERS 969). STEM-EELS data were collected at 300 kV with a current of 60 pA using the direct detection camera (Gatan K2 Summit). More detailed experimental conditions can be found in Supporting Information. A large number of particles as well as different facets of a same primary particle were analyzed to obtain representative data of the whole sample, (see Figure S5 as an example). Collected data were processed by both Multiple Linear Least Square (MLLS) fitting and Principal Components Analysis (PCA) integrated in Digital Micrograph software to identify any differences between the surface and the bulk of the observed primary particles.²⁴ Both procedures gave the same results. EEL spectra were used to quantify the different elements at a nanometric scale. For this purpose, the second derivative of the whole dataset was calculated in order to overcome the problem of overlapping edges, background subtraction difficulties, and to obtain more pronounced signals for Co and Mn (Figure 1), in very small quantity compared to Ni and O (1:1:8:20, respectively). The relative composition profile of the particle can be plotted after performing the MLLS fit on the whole dataset. A detailed description of the method can be found in Supporting Information (Figures S1-S4).

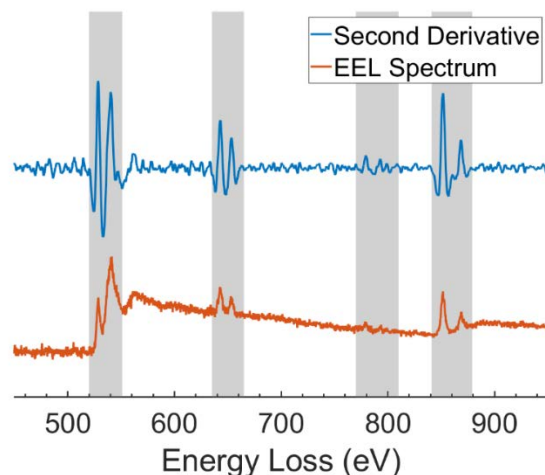


Figure 1. Typical second derivative (blue) of an EEL spectrum (orange) extracted from the very surface of a primary particle. Gray areas indicate O K-edge (around 530 eV), Mn L_{2,3}-edges (around 630 eV), Co L_{2,3}-edges (around 780 eV) and Ni L_{2,3}-edges (around 850 eV).

2.2. NMR spectroscopy

⁷Li MAS NMR spectra were acquired on a Bruker Avance 500 spectrometer ($B_0 = 11.8$ T, Larmor frequencies ν_0 (⁷Li = 194 MHz) at RT. A Bruker MAS probe with a cylindrical 2.5 mm (o.d) zirconia rotor spun at a frequency of 25 kHz was used. Spectra were obtained by applying a single pulse sequence coupled with a pre-scan delay of 10 μ sec before the acquisition of the signal. In this way it was possible to select the surface diamagnetic Li signal only. The paramagnetic Li contained in the AM is indeed characterized by a much faster relaxation time T_2 .²⁵

Since NMR spectroscopy is not an absolute quantitative technique, the realization of a calibration curve was essential in order to successfully quantify surface diamagnetic species. Details are reported in Supporting Information. For the compounds identification based on the isotropic chemical shift (δ), Li₂CO₃ was used as reference at 0.0 ppm.

2.3. XPS Analysis

XPS measurements were conducted on a Kratos Axis Nova Instrument, using a monochromated Al K α source (1486.6 eV) operating at 300 W. The instrument base pressure was 5×10^{-10} Torr and a Pass Energy (PE) of 80 eV was used during the acquisition of the wide-range survey spectra, leading to an instrumental resolution of 0.9 eV. PE of 20 eV at $\theta = 0^\circ$, surface analyzed of $700 \mu\text{m} \times 300 \mu\text{m}$ and 100 meV steps were used instead to acquire high-resolution spectra and exploited to quantify the compounds at the surface of the materials. In this way, it was possible to achieve an instrumental resolution of 0.55 eV measured at Silver Fermi edge. The 3p peaks of the transition metals were acquired together with the Li 1s between 35 and 85 eV in order to have a good background determination and a better quantification of the elements. The background in the Li 1s region was especially designed for that matter and an example can be found in Supporting Information (Figure S9). Spectra of the C 1s (277–300 eV), O 1s (523–537 eV) and S 2p (160–177 eV) were also measured and exploited in the following analysis.

All samples were transferred from the Ar-filled glovebox into the instrument using a dedicated transfer chamber system that was then connected directly to the XPS apparatus, allowing the analysis without letting the materials to be in contact with air.

All data were collected using charge compensation with a low-energy electron gun and calibrated with the adventitious carbon 1s peak at 284.8 eV binding energy. After calibration, all spectra were analyzed using the CasaXPS software (version 2.3.24). The fit was performed using a Shirley type baseline for the background and a pseudo-Voigt function with Gaussian (70 %) – Lorentzian (30 %) for each component. XPS was used in our study to obtain compounds quantification and not as a simple atomic percentage quantification as it is commonly done. The explanation of this quantification method is reported in Supporting Information.

Results and discussion

Cathode materials such as NMCs are typically organized in polycrystalline micrometer-sized particles, namely secondary particles, formed by nanometric single crystals called primary particles. As it can be seen in Figure 2, the primary particles orientation is not always controlled during the synthesis. The importance of these primary particles in the diffusion of Li during cycling was largely demonstrated and their characterization at a nanometric scale became crucial for the comprehension of Ni-rich NMC behavior. In order to obtain and analyze NMC single crystals it was thus important to grind the powder before each characterization. In this way, it was possible to break aggregates and look at individual primary particles. The surface of these primary particles could then be observed, without further modifications from their pristine state. Due to the grinding process, primary particles in the core of secondary particles could not be differentiated from those closer to the surface. The use of local probe analysis techniques, such as TEM, always raises questions about the representativeness of results. For this reason, a large number of primary particles were observed in this study (see Figure S5 as an example). For best clarity, results obtained on representative particles will only be presented in the following sections.

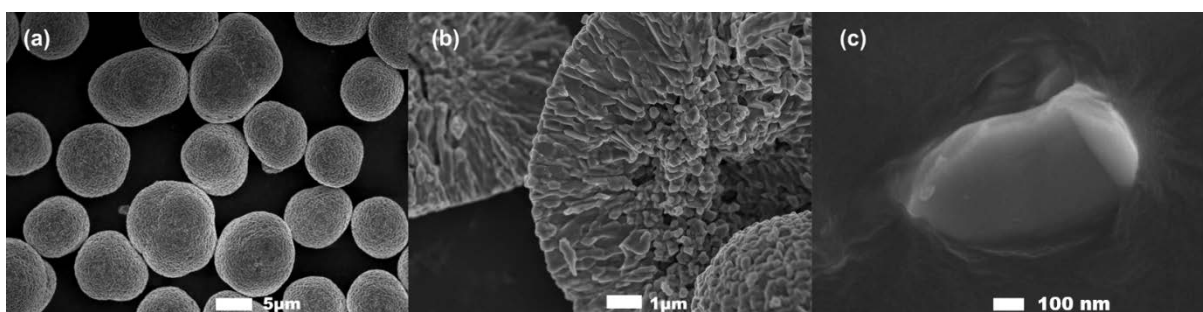


Figure 2. SEM image of the hierarchical microstructure of NMC, from micrometer agglomerates (a) composed of crystallites of few tens of nanometers (b) to primary particles obtained after grinding (c).

3.1 Nanometric characterization of the pristine material

A typical spectrum-image dataset (1 spectrum per pixel) of the pristine powder (Sample A0) is presented in Figure 3a. The two Ni L-edge EEL Spectra used to fit the Spectrum-Image are given in Figure 3b. The orange spectrum appears to be predominant at the surface of the pristine primary particle. It is characterized by a lower intensity of the high energy peak of the L₃-edge split (around 848 eV) when compared to the bulk spectrum (here in blue), resulting in an overall shift of the Ni L-edge maximum towards lower energies. This indicates a reduced state of the Ni at the surface of the pristine powder, closer to a Ni²⁺ ion signal.²⁶

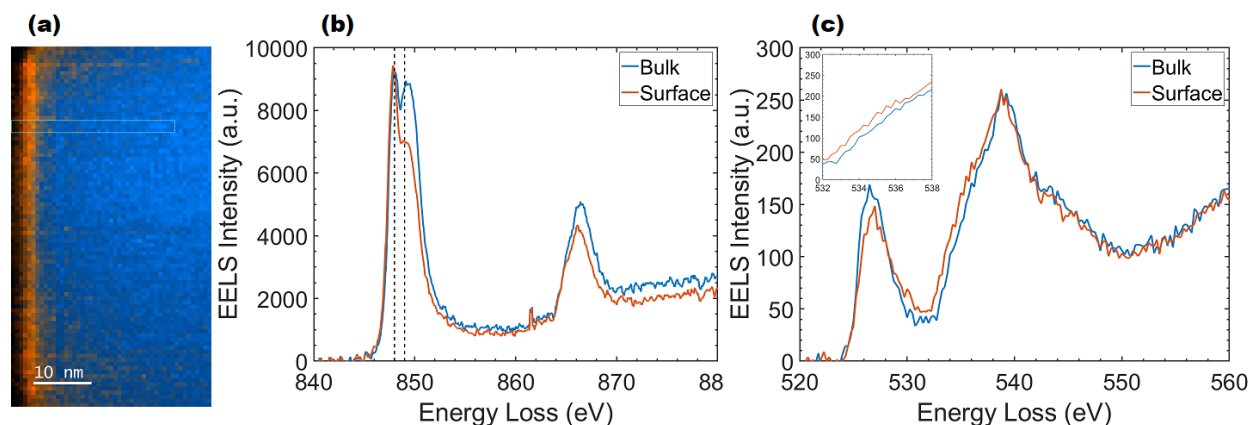


Figure 3. monochromated EELS Spectrum image of A0 sample fitted by MLLS fit (a) using Ni spectra (b) and O spectra (c) from the surface (orange) and the bulk (blue) of an internal zone of a broken secondary particle corresponding to pristine primary particles.

Surface and bulk spectra for the O K-edge are also slightly different (Figure 3c). The shift towards lower energies of the edge around 535 eV (at higher magnification in the inset of Figure 3c) indicates higher electron density (equivalent to a reduction) of the surface oxygen than the bulk one. Ni²⁺ (surface) levels are more destabilized than Ni³⁺ (bulk) ones and tend to form more ionic interactions with surrounding oxygen atoms.²⁷ The resulting higher electron density on

the oxygen levels explains the edge shift towards lower energy. Such interpretation is consistent with the lower pre-edge peak intensity (at around 528 eV) of the surface spectrum than the bulk one. Surface oxygen levels are slightly more filled in electrons, hence allowing fewer transitions to the empty states probed by EELS. Given the surface region limited thickness and an incomplete transformation, it is clear in our mind that these observations should be considered as a qualitative trend and not as a statement of a well-defined “NiO” phase at the surface. Very similar differences between surface and bulk O K- and Ni L_{2,3}-edges fine structures have been already observed, although more pronounced, after long cycling (successive lithiation/delithiation) or water-washing of Ni-rich layered materials.^{21,26}

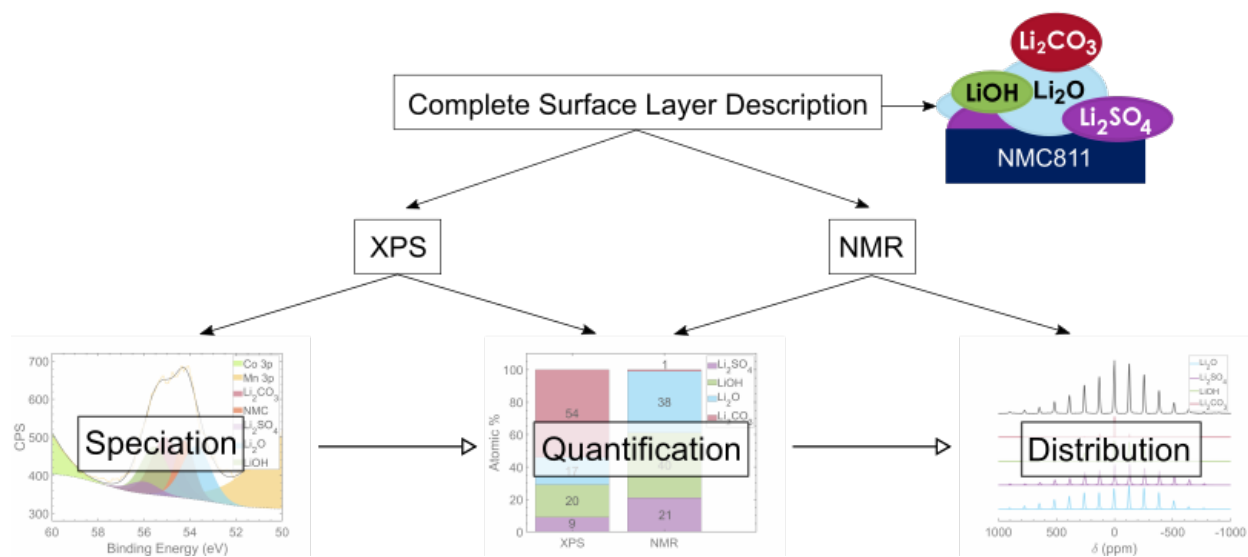
The pristine material, as it arrives from the production plant, is thus already affected by a surface modification. Since these surface features can be related with, or lead to, the formation of impurities, other spectroscopy techniques, namely XPS and MAS-NMR, were exploited to evaluate possible consequences on a larger scale (up to secondary particles). The presence of a peculiar pristine surface layer could indeed be associated with the formation of Li-containing phases that can be well-characterized by these techniques.

3.2. Analysis of the native contamination layer

Essential to the quantification of diamagnetic Li-containing species at the surface of materials, we first exploited high field ⁷Li MAS-NMR. The method introduced in the experimental section and developed in our group by Dupré et al. allows separating the signal of the Li in paramagnetic local environments contained in the AM from the Li in diamagnetic local environments contained in the impurities and/or contamination layer at its surface.^{25,28}

The lithium contained in diamagnetic species at the surface of the pristine material (Sample A0) was found to account for 125 μmol_{Li}/g_{AM} (i.e. 1.2%_{mol}). However, the identification of the various

species contained in the native contamination layer cannot be performed by NMR only. The NMR chemical shifts for the expected surface species, such as Li_2CO_3 and LiOH , are in fact very similar and most lithiated diamagnetic impurities are measured within -1.1 to 4.0 ppm. Consequently, XPS was used to provide for a more exhaustive description of the speciation of surface species in order to ensure a deconvolution of the ^7Li MAS-NMR isotropic band around 0.0 ppm. The description of this powerful method coupling MAS-NMR and XPS is summarized in Scheme 1.



Scheme 1. Method used for the complete description on the surface contamination layer.

XPS spectra of the pristine Sample A0 are shown in Figure 4 and all XPS quantitative data are gathered in Table 2. The C 1s spectrum (Figure 4a) shows the hydrocarbon surface contamination component (C–C, C–H) at 284.8 eV, commonly detected on sample surfaces. Other signals corresponding to species with doubly bounded oxygen functionalities (at 287.2 eV) and ester functions (at 288.2 eV) were also used to deconvolve the adventitious carbon signal.

An important signal at 289.7 eV was assigned to the carbonate function, here considered as Li_2CO_3 , a typical contaminant at the surface of NMC materials. A carbonate signal was detected

as well on the O 1s peak (Figure 4b) at 531.3 eV and on the Li 1s peak at 55.2 eV (Figure 4d), confirming the presence of Li_2CO_3 .

The S 2p peak (Figure 4c) is split into two components ($\text{S } 2p_{1/2}$ and $\text{S } 2p_{3/2}$ with an area ratio of 1:2) because of the spin orbit coupling effect. The peak position (168.9 eV for the $\text{S } 2p_{3/2}$) is typical of the sulfate $(\text{SO}_4)^{2-}$ group. These sulfates are attributed to residuals from the synthesis and could correspond to lithiated species or not.

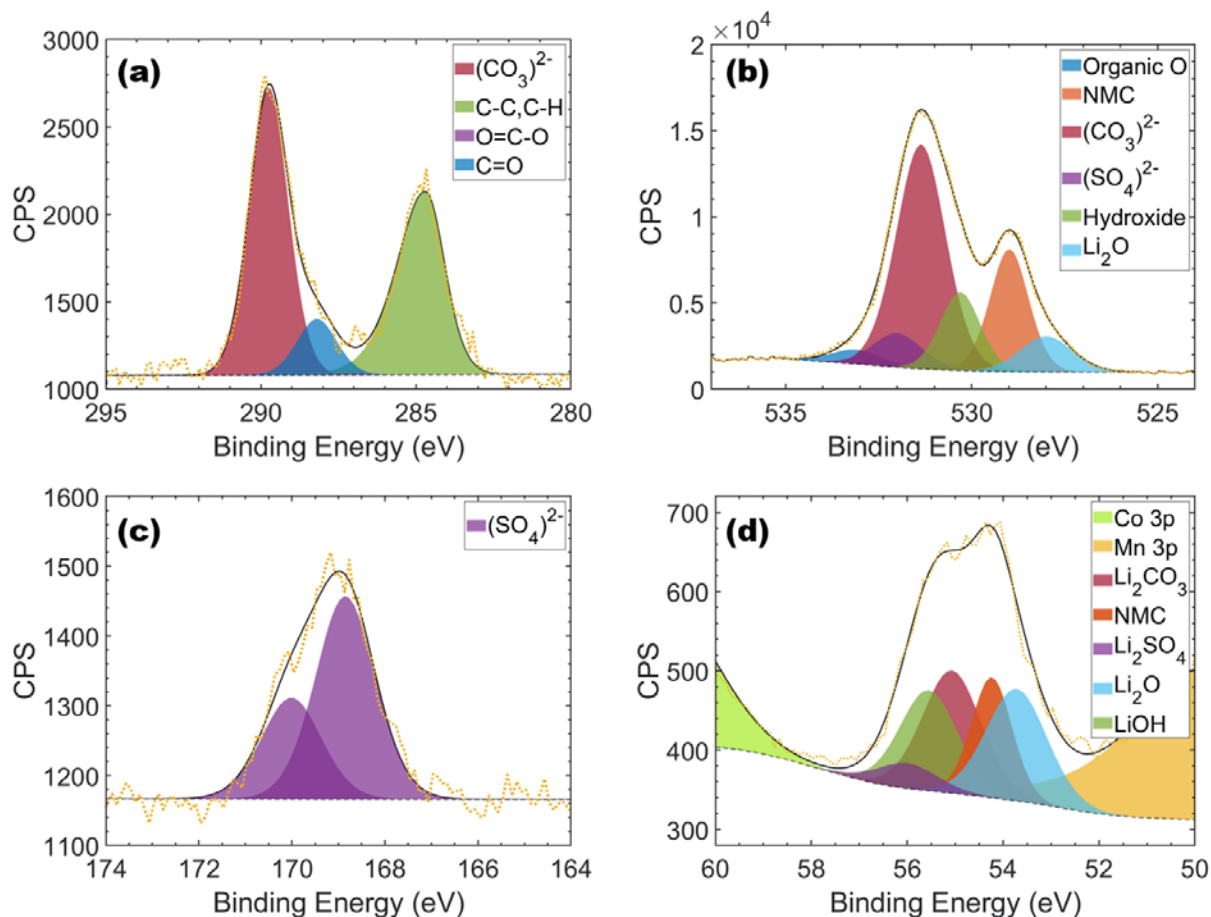


Figure 4. XPS C 1s (a), O 1s (b), S 2p (c) and Li 1s (together with Ni 3p, Mn 3p and Co 3p in (d)) spectra of A0 pristine sample. Experimental data are represented in yellow dashed line and the fit result in straight black line. 3p peaks for Ni, Co and Mn are modeled for deconvolution purposes but their intensity is not exploited.

Unlike the C 1s peak, the deconvolution of the O 1s peak (Figure 4b) is more complicated since distinct components are not clearly visible, except for NMC (529.0 eV) and Li₂O at 528.0 eV. Additional contributions on the O 1s spectrum were deduced from oxygen containing species identified in the previously analyzed C 1s and S 2p high-resolution spectra and included in the fit. It was thence possible to identify one component corresponding to (SO₄)²⁻ at 532.0 eV thanks to the previous fit of the S 2p peak. One component gathering all the organic compounds at 533.1 eV was also added to the fit, together with the one corresponding to the carbonate function as explained earlier. Constraints on the integrated areas were imposed as described in Supporting Information.

Table 2. Binding Energy (eV), FWHM, atomic percentages (%) and assignments of C, O, S and Li peaks from XPS spectra of pristine NMC811 powder.

Orbital ¹	B.E. (eV)	FWHM (eV)	Atomic %	Peak assignment ²⁹
C 1s	284.7	1.5	6.7	C–C, C–H
	286.0	1.5	0.0	C–OH, C–O–C
	287.2	1.5	0.1	C=O
	288.2	1.5	1.6	O–C=O
	289.7	1.5	8.2	Li ₂ CO ₃
Total C			16.6	
O 1s	528.0	1.7	4.3	Li ₂ O
	529.0	1.2	10.9	NMC
	530.3	1.3	7.2	LiOH

¹ Ni 3p, Co 3p and Mn 3p peaks were used here only for a better deconvolution of the Li 1s signal. B.E. and FWHM for these elements are thence not physically significant and so not reported in the Table and not further discussed. Atomic percentages were recalculated and normalized after subtracting transition metal signals.

	531.3	1.6	25.5	Li ₂ CO ₃
	532.0	1.6	3.9	Li ₂ SO ₄
	533.1	1.6	1.4	Organic compounds
Total O			53.2	
S 2p_{3/2}	168.9	2.4	0.6	Li ₂ SO ₄ ³⁰
S 2p_{1/2}	170.0	2.4	0.3	Li ₂ SO ₄
Total S			0.9	
Li 1s	53.8	1.4	8.2	Li ₂ O
	54.3	1.4	5.6	NMC
	55.2	1.5	7.1	Li ₂ CO ₃
	55.2	1.5	6.4	LiOH
	55.9	1.4	2.0	Li ₂ SO ₄
Total Li			29.3	
Total			100.0	

However, these components alone could not fully explain the experimental O 1s spectrum. As a consequence, an additional component was to be considered at 530.3 eV. The integrated area of this contribution, corresponding to the hydroxide function, was let free to obtain the best fit. This same method was used to decompose the Li 1s core peak (Figure 4d) into 5 contributions, discernible only by using this approach. Li₂O (deduced from the O 1s peak) can be found at 53.8 eV, slightly superimposed with the component at 54.2 eV, corresponding to Li ions intercalated in the NMC. For simplification purpose, all the sulfates were hypothesized to be Li₂SO₄ and a peak was thence fixed at 55.9 eV to represent this compound. On the other hand, it was trickier to make the difference between lithium carbonate and hydroxide. Some references were analyzed by XPS, evidencing a very similar peak position for the two compounds

(Figure S6). For this reason, two different components at 55.2 eV were used to represent Li_2CO_3 and LiOH . The fit was here performed by constraining the LiOH Li 1s peak integrated area in relation to the corresponding LiOH signal in the O 1s spectrum. Li_2CO_3 integrated area was instead let free from any constraints, since the carbonate amount was the only one not consistent with the ^7Li MAS-NMR quantification, as it will be detailed later.

Once Li_2CO_3 , LiOH , Li_2O and Li_2SO_4 were identified by XPS as the principal surface lithiated species, this information was integrated into the fit of the ^7Li MAS-NMR spectrum, representing the contributions of Li nuclei in various diamagnetic environments. The deconvolution of the isotropic resonance corresponding to the pristine powder is shown in Figure 5 and the experimental isotropic chemical shifts (δ) and FWHMs corresponding to each diamagnetic compound are summarized in Table 3. δ values of the four identified compounds are given as a difference with respect to Li_2CO_3 , used here as a reference. These values were set by taking into account the ones calculated by Kösher et al.³¹ A good fit was obtained by using one component at 4.0 ppm (Li_2O), one at 1.8 ppm (LiOH), one at 0.0 ppm (Li_2CO_3) and one at -1.1 ppm for Li_2SO_4 . Once these chemical shifts were identified and used for the deconvolution and the fit of the pristine spectrum, they were fixed for all the other analyzed spectra (e.g., spectra corresponding to aged samples), letting FWHMs and the intensities free to change.

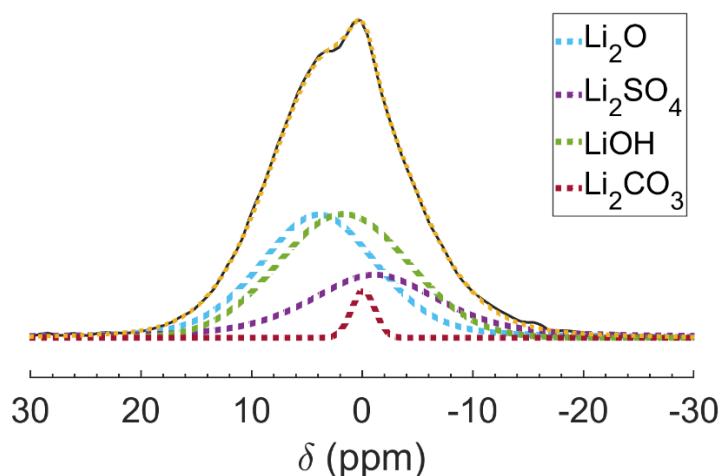


Figure 5. ^7Li MAS-NMR spectrum of pristine A0 powder (black) fitted using four contributions: Li_2O (light blue), Li_2SO_4 (purple), LiOH (green) and Li_2CO_3 (red). The sum of the different contributions is represented by the yellow line.

As it can be seen in Figure 5, while the peak corresponding to Li_2CO_3 , at 0.0 ppm, is very sharp (FWHM = 2.4 ppm), all the other contributions are much broader (Table 3). This sharp signal suggests the formation of a well-defined Li environment in Li_2CO_3 (narrow distribution of environments) as well as further distance from the surface of the paramagnetic material (weaker Li nucleus-electron dipolar interaction) than the other detected lithiated species. A more disordered environment as well as a closer intimacy with the AM would be expected in the case of the formation of Li_2CO_3 from the direct reaction of the surface of the AM with the surrounding atmosphere (even though controlled). The formation of well-defined and separated Li_2CO_3 as a secondary product —hence further away from the surface—, is in better agreement with the observed sharper NMR signal.

Table 3. Isotropic Chemical Shift δ (ppm) and FWHM of the contributions used for the deconvolution of ^7Li spectrum of pristine NMC811 powder.

Compound	δ (ppm)	FWHM (ppm)
Li_2SO_4	-1.1	13.9
Li_2CO_3	0.0	2.4
LiOH	1.8	13.9
Li_2O	4.0	12.3

The larger FWHM of Li_2O , Li_2SO_4 and LiOH signals compared to that of Li_2CO_3 reported in Table 3, could be both due to a higher disorder in the Li environment and to a higher proximity to the paramagnetic surface of the NMC material. This intimacy indeed leads to a faster T_2^* relaxation time and thus to a broader line width. The analysis of the intensity distribution of these four contributions over the spinning side bands helped us confirming the second explanation. Larger sideband manifolds, like those shown in Figure 6c-e for Li_2O , Li_2SO_4 and LiOH are in fact typical of a stronger electron-nucleus dipolar interaction between the observed Li nuclei and the paramagnetic centers of the NMC. Li_2CO_3 , having a small 155 ppm FWHM of the sideband manifold (Figure 6b), is therefore submitted to a much weaker dipolar interaction. Such an interaction decreases quickly with the distance (typically as $1/r^3$, where r is the distance between the observed nucleus and the paramagnetic center),²⁵ and suggests that Li_2CO_3 is the further away from the bulk material.³² The compound LiOH seems to be present at an intermediate distance, while Li_2SO_4 and Li_2O are the closest to the bulk material. Li_2SO_4 and Li_2O are typical “native” impurities, straight from the synthesis. Li_2SO_4 is the expected form of sulfur, which is often detected by ICP performed on the pristine powder, because of the sulfate based precursors. Li_2O has often been considered as the form of residual lithium after calcination.^{9,33}

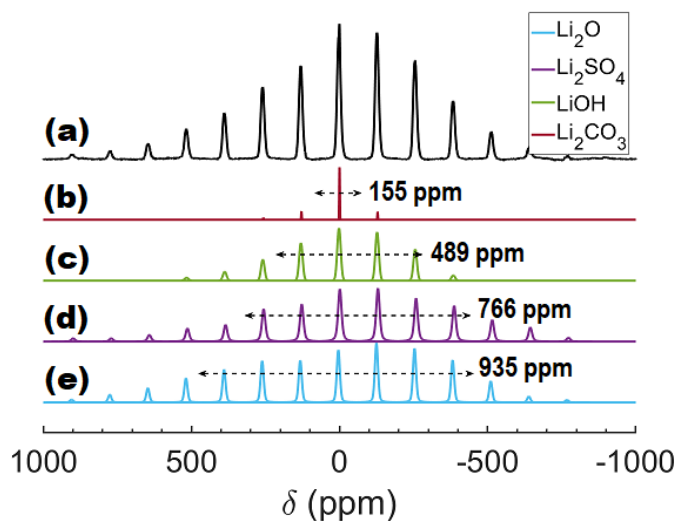


Figure 6. ^7Li MAS-NMR spectrum of pristine powder (a) and distribution of the intensity of each contribution (Li_2CO_3 in red, LiOH in green, Li_2SO_4 in purple and Li_2O in light blue) over the spinning side bands (b-e). Spectra b-e are normalized with respect to the intensity of the isotropic resonances and indications of the FWHM of the sidebands manifold are given for each contribution.

The results for the quantification of the native contamination layer performed by both XPS and NMR are shown in Figure 7. For the XPS data presented here, the components of NMC, residual hydrocarbon and adventitious carbon contaminations were excluded in order to compare solely the species that are measurable by both techniques. MAS-NMR based on ^7Li nucleus obviously detects only surface diamagnetic lithiated species (a complete XPS quantification can be found in Table 2). Clear differences can be seen between the two quantification measurements. Li_2O , LiOH and Li_2SO_4 quantities seem to be underestimated when calculated by XPS, while the amount of Li_2CO_3 is largely overestimated. These two techniques are in fact sensitive to different parts of the sample. While the NMR analyses the whole sample, XPS is limited by the spot size ($700 \times 300 \mu\text{m}$) and by the sampling depth, typically around 5 nm. XPS is thence not representative of the whole sample, but only of the extreme surface of the analyzed area. Moreover,

one has to keep in mind that the composition and thickness of the native contamination layer are expected to vary significantly from one place to another over the spot size. The coupling with NMR is therefore a major asset in this study, considering that XPS is usually one of the most common tools used to analyze NMCs surface chemistry in the literature.

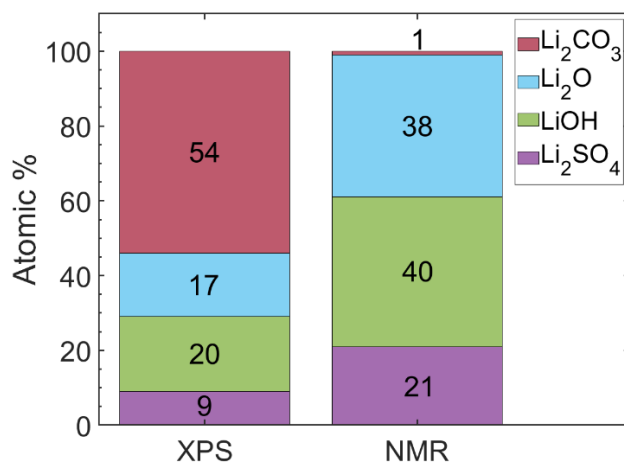


Figure 7. Quantification ($\pm 10\%$) of the native contamination layer on pristine ground powder determined by both XPS and NMR. Phase percentages for Li_2CO_3 (red), Li_2O (light blue), LiOH (green) and Li_2SO_4 (purple) are indicated.

The difference in the Li_2CO_3 quantification, representing only 1% in the NMR quantification (that is $0.4 \mu\text{mol/g}_{\text{AM}}$) *versus* 54% in XPS, can be explained considering that this compound is mostly formed at the very surface of the sample (as demonstrated by the dipolar interaction study in the MAS-NMR signal, Figure 6) and is situated on the external part of the pristine interphase. XPS quantification thus overestimates the Li_2CO_3 percentage largely. It is however quite interesting that the respective proportions of Li_2O , LiOH and Li_2SO_4 are found to be very similar in both techniques. Ratios $\text{LiOH}/\text{Li}_2\text{O}$ and $\text{Li}_2\text{SO}_4/\text{Li}_2\text{O}$ are indeed close to 2 and 0.5, respectively. From the good agreement between these two analysis techniques, it can be deduced that even if Li_2O , Li_2SO_4 and LiOH are stacked (in this order) from the NMC surface, this distribution suggested by

NMR should not be seen as well-defined successive layers. Hence, XPS results help us mitigating the oversimplified vision of an ideal layered surface suggested by NMR.

The reasoning above is based on the fact that all surface species detected by XPS are also detected by NMR. Considering that ^7Li MAS-NMR only was used, surface species not containing lithium will be missed by MAS-NMR. A deeper examination of XPS quantification values on the carbonate reported in Table 2, shows that the ratio $\text{Li}_{(\text{Li}_2\text{CO}_3)} / \text{C}_{(\text{Li}_2\text{CO}_3)}$ results to be 0.9 / 1 instead of the expected 2 / 1 that would be obtained if all carbonates were fully lithiated. Other carbonate sources may thus be present at the material surface, such as LiHCO_3 and/or $(\text{TM})\text{CO}_3$. Fits, detection limits and characteristics of XPS and NMR techniques did not allow us to go deeper in this determination. The possible existence of transition metal carbonates is a very valuable piece of information, considering that this hypothesis was already proposed by Jung et al.. This group suggested the extraction of Ni from the NMC811 surface to form part of the contamination layer upon storage in ambient conditions.²⁰ However, in our pristine powder (not an electrode as in their work), the quantity of such transition metal carbonates appears to be quite small when XPS and NMR results are combined. As a matter of fact, if we make the hypothesis that the composition found by XPS is representative of the average composition of the surface lithiated layer, approximately 50% of the carbonates would be under the form of $\text{TM}(\text{CO}_3)$. This would mean that Li_2CO_3 and $\text{TM}(\text{CO}_3)$ would be in the same amount of around $0.6 \mu\text{mol/g}_{\text{AM}}$, i.e. 0.007%_{wt}. This represents roughly 10 times less than the quantity they deduced by gas chromatography on the fresh electrodes.

3.3. Nanometric quantification at the primary particle surface

The presence of transition metal impurities in the contamination layer suggested by XPS and MAS-NMR analyses could imply the modification of the NMC811 extreme surface TM

composition (over a few atomic layers). In order to determine whether such a variation can be evidenced at the primary particles surface, the pristine powder was analyzed by both STEM-EDX and STEM-EELS, the sole techniques with sufficient spatial resolution. This is a quite challenging task since any sample preparation that would be too harsh on the material chemistry would affect any conclusion. For this reason, we chose to simply crush in a mortar the pristine secondary particles. The following results thus reflect surfaces of primary particles situated either in the core or at the surface of the secondary particles, the latter ones being more exposed to the external atmosphere but in lesser amount than the former ones.

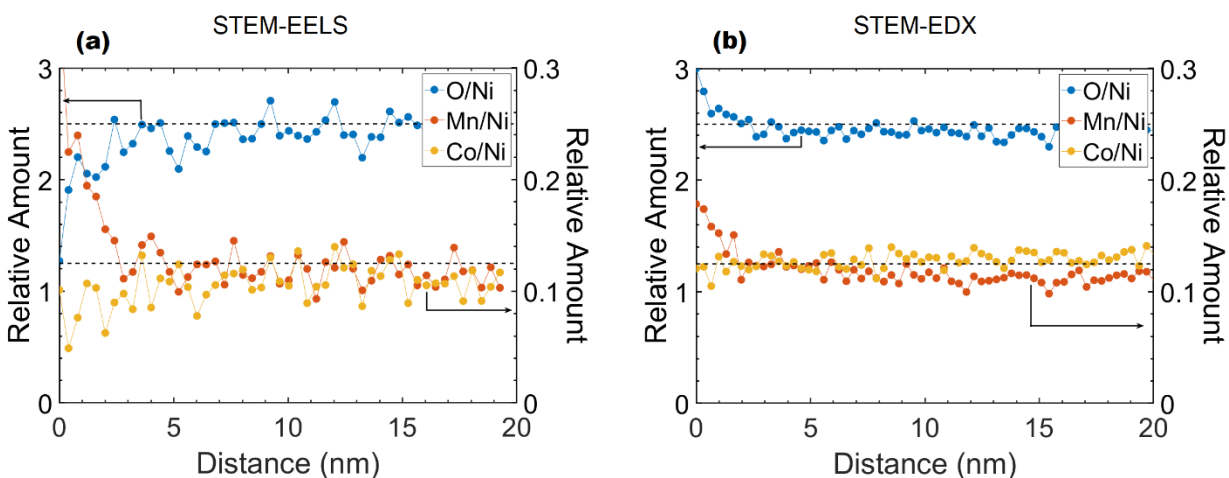


Figure 8. Calculated ratios for A0 pristine sample: O/Ni (blue), Mn/Ni (orange) and Co/Ni (yellow) from (a) STEM-EELS and (b) STEM-EDX data. Theoretical bulk values are indicated by the dashed black line and are 2.5 and 0.125 for O/Ni and TM/Ni, respectively.

The ratios Mn/Ni, Co/Ni and O/Ni calculated from the STEM-EELS pristine powder spectra (Sample A0) are represented in Figure 8a as a function of the distance from the beginning of the AM primary particle surface (0 nm). A detailed description of the method can be found in the Supporting Information file. This same analysis was performed on many particles of different

shapes and with different crystalline orientations, always obtaining similar results. Our method does not rely on a lengthy and possibly biased crystal orientation procedure and thus allows measurements on dozens of surfaces (Figure S5). Figure 8a is thus quite representative of the pristine sample surface state. Since these analyses were obtained after binning all the pixels at the observed surface, they represent an average over hundreds of nanometers. This method necessitating the use of a reference element, Ni was used here as such, being the one with the higher signal to noise. Surface composition in Figure 8a is thus given with respect to Ni. The elemental composition was measured to be quite stable within the bulk of the primary particles (beyond ~5 nm). Closer to the external surface, variations were observed. Considering that Mn/Ni, Co/Ni and O/Ni ratios behave quite differently when approaching the surface, the variations cannot be interpreted as due to a Ni depletion (or increase) only. Compositional changes were found to exist within the first 3 nm of the AM primary particles surface.

Firstly, the surface appears to be oxygen deficient with respect to nickel. Even if only a trend can be asserted here, the ratio tends towards 1. This value is in line with the hypothesis of an extreme surface of the AM primary particles (thickness inferior to 1 nm) —the surface in direct contact with the atmosphere and, potentially, the electrolyte— approaching to a NiO phase. This analysis is consistent with our previous observation of the surface Ni oxidation number reduction towards a Ni^{2+} state resulting from the Ni-L_{2,3} fine structure measurements. Similarly, it is also in line with affirmations found in the literature.^{34,35} However, the lower surface oxygen content is not compatible with the presence of NiCO_3 in the contamination layer.²⁰

Secondly, a Mn enrichment is clearly visible at the AM extreme surface. To the best of our knowledge, such an unexpected result has never been reported before. One could argue that a nickel depletion (e.g. to form new compounds in the contamination layer) would also result in the

observation of a Mn enrichment, since ratios and not absolute values are reported here, but this would be inconsistent with the rather stable Co/Ni ratio. This debate can also be overcome thanks to the STEM-EDX measurements. In this case, the percentages of the 4 elements (oxygen and TMs) can be obtained without necessitating a reference element. For the sake of comparison with EELS, the resulting calculated ratios are presented in Figure 8b. The same Mn amount increasing trend was measured (Co quantity being roughly constant until the extreme surface). In spite of the different detection methods (inelastically transmitted electrons or emitted X-rays), results are consistent. However, it should be mentioned that a lower surface oxygen content was not detected by STEM-EDX. Since the oxygen K_{α} emission energy (0.5 keV) is much lower than the one of transition metals (from 5.9 keV to 7.5 keV), absorption corrections affect greatly the oxygen percentage determination. Despite the use of four EDX detectors, the varying orientations of the crystal surfaces with respect to them cannot be totally compensated. Furthermore, the presence of high oxygen content compounds such as LiOH and/or carbonates cannot be excluded. Nevertheless, such a limitation has a little effect on the high energy transition metal peaks. The surface Mn enrichment (50 to 100% increase vs. bulk composition, Figure 8) can thus be confirmed. A last comment on these results should be that no variability could be evidenced as a function of the surface crystallographic planes, suggesting that an extreme surface of pristine primary particles presents this divergence from the nominal bulk composition.

Following the work of Jung et al. showing the formation of nickel based carbonates after storage, a strongly nickel deficient surface would be more logical.²⁰ Other authors found instead a Co content increasing at the extreme surface.¹⁶ We may suggest that this Mn enrichment is a consequence of different surface phases stabilities during the synthesis rather than being related to storage. Thermodynamic data were gathered by Shurtz et al. for LiMnO_2 , LiCoO_2 and LiNiO_2 .³⁶

Despite the important lack of thermodynamic data for these compounds, we can roughly assume that oxide stabilities are correlated with their formation enthalpies (enthalpies of mixing should here be neglected).³⁷ Experimental formation enthalpies for LiNiO₂, LiCoO₂ and LiMnO₂ at 298 K are -593.0, -679.6 and -839.5 kJ mol⁻¹, respectively. A significant difference between Ni, Co and Mn based oxides can be noticed. Since a high temperature step is necessary for the formation of the desired NMC811 phase, the observed Mn enrichment could result from the higher stability of a Mn-rich surface in NMC layered materials. The Mn excess would not need to be compensated by a departure of Ni and Co from the AM surface, but it could be provided by a negligible (and unmeasurable) Mn composition gradient from the core of the primary particles. We have not found a detailed theoretical study that would neither contradict nor validate this suggestion.

The above AM extreme surface analyses revealed a nickel reduced oxidation state and a Mn enrichment. Since they might be correlated or not, submitting the material to an accelerated aging could help us determine which are the conditions controlling their advent.

3.4. Influence of storage conditions

The pristine NMC powder studied till now was then stored in specific conditions to obtain samples A1 and A2, after 15 minutes and 2 days in RH = 30%, respectively, as detailed in Experimental Section (see Table 1). The aim was here to exacerbate reactions occurring at the NMC surface in order to determine whether small amounts of water vapour could initiate the transformations previously observed. Specific RH storage conditions have already been shown to result in the formation of various species, such as Li₂CO₃.^{20,38} Based on our previous detailed study, we used ⁷Li MAS-NMR and XPS to characterize and quantify the lithiated species at the NMC surface after storage. Moreover, since the extraction of lithium from the material is expected

to occur together with a change in the TM oxidation state, STEM-EELS experiments were carried out to confirm this hypothesis and to determine its extent.

As for the previous data analysis on A0 pristine powder, two components were used to fit A1 and A2 Ni L_{2,3}-edges Spectrum-Images (Figure 9). Each pixel can be described as a combination of a surface (Ni in a more reduced state) and a bulk (mainly Ni³⁺) spectrum. Coefficients were normalized to be able to compare their evolution from the surface, but their absolute values were much smaller at the surface, due to the reduced thicknesses.

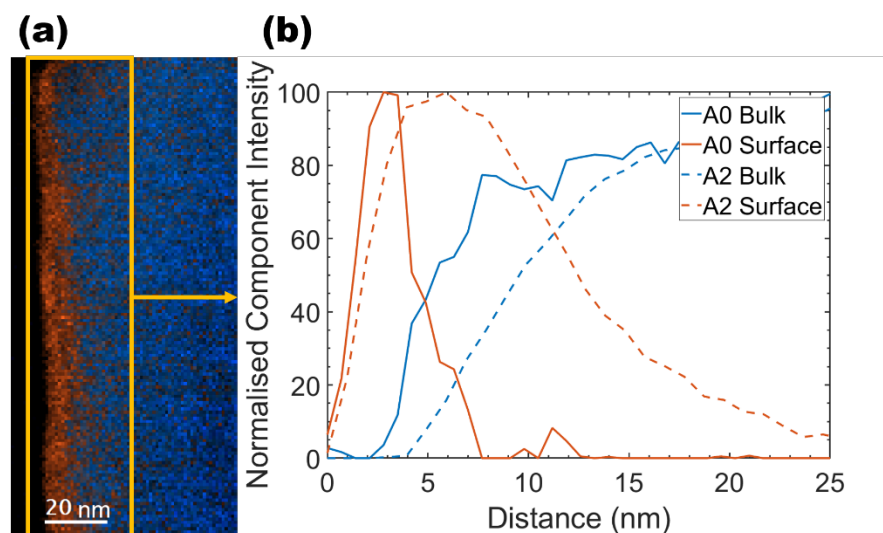


Figure 9. (a) EEL Spectrum-image of A2 sample after MLLS fit and (b) comparison for A0 (straight line) and A2 (dashed line) samples of surface (orange) and bulk (blue) contributions as a function of the distance from the beginning of the particle surface.

The surface component (orange full line) becomes negligible around 7 nm from the beginning of the surface in the pristine sample A0; the bulk component is then predominant. The thickness of this reduced Ni layer increases up to 15-20 nm in the sample aged for two days in RH 30% (orange dotted line). The phase change is thus clearly extended further inside Sample A2 than in the pristine material (Sample A0). The fine structures at the edges were found to be very similar in Samples A0 and A2. This phase change was found to be associated with a lithium extraction

from the AM, as proven by ^7Li MAS-NMR measurements. As a matter of fact, the total lithium contained in the diamagnetic species at the surface of the NMC increases significantly from $117 \mu\text{mol}_{\text{Li}}/\text{g}_{\text{AM}}$ to $148 \mu\text{mol}_{\text{Li}}/\text{g}_{\text{AM}}$ and $176 \mu\text{mol}/\text{g}_{\text{AM}}$ when going from Sample A0 to A1 and A2, respectively (see Table 1 for samples description).

The evolution upon storage of each diamagnetic compound (Li_2SO_4 , LiOH , Li_2O , Li_2CO_3) measured quantities ($\mu\text{mol}/\text{g}_{\text{AM}}$) is presented in Figure 10. Our method allowed demonstrating that Li_2SO_4 and Li_2O amounts remain nearly constant, while a large Li_2CO_3 and LiOH increase was measured. Li_2SO_4 and Li_2O not being affected by the storage conditions, their presence could be interpreted as stemming from initial synthesis residuals. This result further validates our analytical strategy and points at LiOH and Li_2CO_3 as the essential coupled products of the NMC811 surface reactivity. It should be stressed that MAS-NMR quantities are multiplied by ~ 2 and ~ 30 for LiOH and Li_2CO_3 respectively after 15 minutes of exposure only (sample A1). This result suggests an extremely fast reaction time. Even if our samples were exposed to much higher relative humidity in our experiments than in industrial dry room (and still sensibly lower than in other studies), our results indicate a hypersensitivity of the NMC811 bare surface to the $\text{H}_2\text{O}/\text{CO}_2$ atmosphere.

The greater increase in carbonate compared to the hydroxide amount could be explained by the carbonate being the end product of the surface change. The reaction $2\text{LiOH} + \text{CO}_2 \rightarrow \text{Li}_2\text{CO}_3 + \text{H}_2\text{O}$ is thus instrumental to the observed change. The LiOH could be —at least partially— formed according to the suggested reaction:



This reaction would also justify the presence of reduced Ni at the NMC811 surface.

The hydroxide quantity only doubles again (from 68 to $112 \mu\text{mol}/\text{g}_{\text{AM}}$) after 2 days (Sample A2). Similarly, the carbonate amount doubles after the same period of time (Sample A2), the formation

paths being linked between the two. At the beginning of exposure, the surfaces are relatively fresh and the new phase identified on the pristine material (similar to NiO) is not thick enough to prevent a fast reaction with atmosphere to form new LiOH and Li₂CO₃. A further progression of the reaction front is then more difficult in presence of the 10 nm layer measured in Figure 9b. A slower Li₂CO₃ and LiOH formation rate is thus consistent with the new observed interphase.

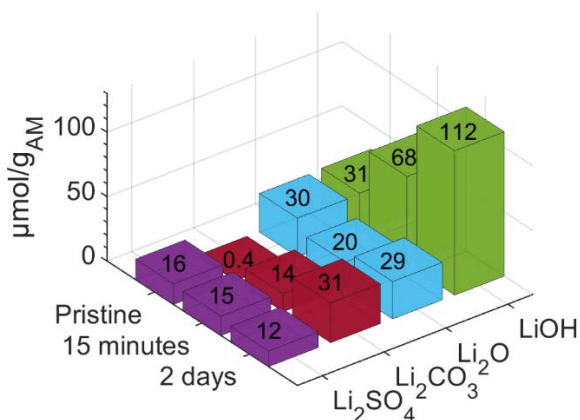


Figure 10. Quantity of lithiated species ($\pm 10\%$) detected by ^7Li MAS-NMR at the AM surface for the pristine (A0), A1 (15 minutes) and A2 samples (2 days in RH = 30%). Li₂SO₄ (purple), Li₂CO₃ (red), Li₂O (blue) and LiOH (green).

The Li₂CO₃ ^7Li MAS-NMR signal gives further information about its localization. The signal broadening (Table 4) implies that the formation of the new carbonate species (Samples A1 and A2) is situated closer to the AM surface when compared to Sample A0. The intensity distribution on the spinning side bands indeed increases upon aging. It could be interpreted as a consequence of this new Li₂CO₃ formation on the relatively fresh NMC surface obtained after grinding. The Li₂O linewidth and intensity distribution over the spinning sidebands remain nearly constant, indicating that the original Li₂O on the pristine sample (A0) is unaffected by the large surface modifications described above. XPS experiments confirmed these conclusions. The Li₂CO₃ signal represents 95% of the lithiated compounds in sample A2 (Figure S7). Other species become

extremely difficult to quantify. The newly created Li_2CO_3 is thus most probably present in the form of an extended layer of ~ 10 nm thickness masking the underlying LiOH. The sequence NMC/LiOH/ Li_2CO_3 is further confirmed by the measurement of a larger FWHM of the LiOH ^7Li MAS-NMR signal compared to that of Li_2CO_3 , again indicative of a LiOH higher proximity with the active material.

Table 4. Parameters from ^7Li MAS-NMR signal features for A0, A1 and A2 samples.

	δ (ppm)	FWHM (ppm)	I isotropic resonance %
A0			
Li_2SO_4	-1.1	14	15
Li_2CO_3	0.0	2	74
LiOH	1.8	14	25
Li_2O	4.0	12	13
A1			
Li_2SO_4	-1.0	12	15
Li_2CO_3	0.0	5	25
LiOH	1.7	12	17
Li_2O	4.0	13	13
A2			
Li_2SO_4	-1.1	13	19
Li_2CO_3	0.0	7	18
LiOH	1.7	14	15
Li_2O	4.0	12	15

Moreover, as for the A0 pristine sample, XPS fits on samples A1 and A2 were performed in order to evaluate the possible quantity of carbonates other than Li_2CO_3 . It appears that the Li and

C amounts corresponding to the carbonate are very close to the expected values of a phase Li_2CO_3 (C 1s and O 1s peaks, Figure S8) in samples A1 and A2. This would mean that species like LiHCO_3 or transition metal carbonates become minority phases after aging in humid air. Such finding is consistent with the idea that the newly created and thicker lithium carbonate is formed on an increasingly thick LiOH layer and could not interact anymore (if any) with transition metals of the surface.

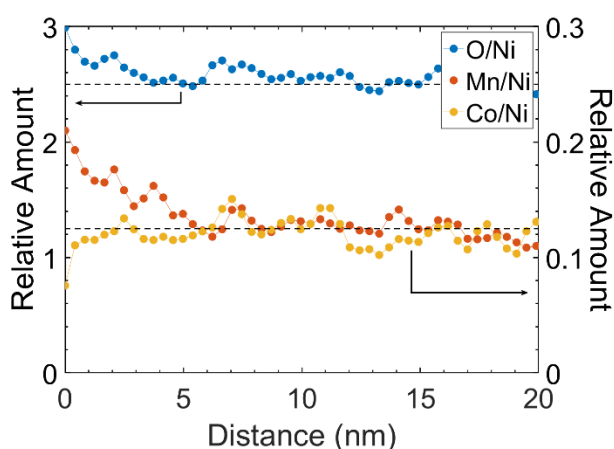


Figure 11. Calculated ratios for A2 sample: Co/Ni (blue), Mn/Ni (green) and O/Ni (red) as measured by STEM-EELS. Theoretical bulk values are indicated by the dashed black line and are 2.5 and 0.125 for O/Ni and TM/Ni, respectively.

Finally, Samples A1 and A2 surface compositions were investigated by STEM-EELS to inquire on the effect of short-term storage on the surface element quantifications. The results for the TM quantification of aged materials were very similar to those obtained one on the pristine sample A0 (Figure 11). A small (~5 nm) surface Mn enrichment was measured. Despite the higher RH atmosphere samples A1 and A2 were subjected to, despite the increased reduced Ni surface layer and the important formation of LiOH compared to Sample A0, these changes are taking place without major relative TM compositional modifications and are thus not strong enough to promote

a selective diffusion of TMs. Figure 11 also shows that the oxygen amount decrease at the surface is less significant than in the pristine material (Sample A0). As a matter of fact, the oxygen content can often be found to be above the nominal bulk value. This result is due to the contamination (mainly oxygen-carbon based) that considerably occurs on these exposed to humid air samples. Surface contamination is a well-known consequence of such treatment.

3. Conclusion

We presented in this study a complete characterization of a pristine industrial grade NMC811 powder, down to the sub-nanometer level, providing a possible explanation for its behavior during storage in defined short-term and low-humidity conditions. A multi-analytical approach based on on-site characterization techniques was used to give a complete picture of the material at different scales. The lithium contained in diamagnetic species at the surface of the pristine material (Sample A0) was found to account for 1.2%_{mol} by MAS-NMR and to account up to 1.5%_{mol} and 1.7%_{mol} upon storage in the studied conditions (Samples A1 and A2 respectively). Such species were identified to be Li₂O, Li₂SO₄, LiOH and Li₂CO₃ (from the closest to the furthest from the surface of the active material). Li₂CO₃ is found in minor proportion but its amount increases faster after exposure to humid air. By combining both MAS-NMR and XPS, it was possible to quantify the evolution of the lithiated species and their distribution from the surface. This allowed us to propose a succession of reactions taking place at this surface and to stress its hyper reactivity even towards minute amounts of H₂O. The lithium extraction from the material to the surface layer was demonstrated to be accompanied by a progressive reduction of the surface nickel, tending to form NiO, as evidenced by the STEM-EELS data acquired in monochromated mode. STEM-EDX and STEM-EELS were then used to monitor the composition trend within the first atomic layers of the active material through the quantification of oxygen and transition metals at a nanometric scale,

showing a Mn enrichment at the surface, not dependent on the storage conditions and therefore probably coming from the synthesis.

ASSOCIATED CONTENT

Supporting Information..

The Supporting Information is available free of charge at.

Additional experimental details for STEM-EELS. Description of the second derivative method for elemental quantification of transition metal. Examples of such quantification over many primary particles. Description of methods for ^7Li MAS-NMR quantification and XPS compounds quantification. XPS reference spectra for LiOH and Li_2CO_3 . Data fit in the 47-75 eV range for A2 sample. Example of the background developed for the Li 1s XPS region (PDF)

AUTHOR INFORMATION

Corresponding Author

*Philippe Moreau, Nantes Université, CNRS, Institut des Matériaux de Nantes Jean Rouxel, IMN, F-44000 Nantes, France; <https://orcid.org/0000-0002-1691-1592>; Email: Philippe.Moreau@cnrs-imn.fr

Author Contributions

The manuscript was written through contributions of all authors. All authors have given approval to the final version of the manuscript.

Acknowledgement

Funding by the French Contrat Plan État-Région and the European Regional Development Fund of Pays de la Loire, the CIMEN Electron Microscopy Center in Nantes, is greatly acknowledged. The authors thank Dr. Rabeb Grissa for her help in the compound-based analysis procedure for XPS experiments. The authors thank Dr. Vincent Fernandez for his precise determination of the XPS background in the lithium region. The authors also thank Dr. Eric Gautron for his help in the monochromated STEM-EELS experiments.

References

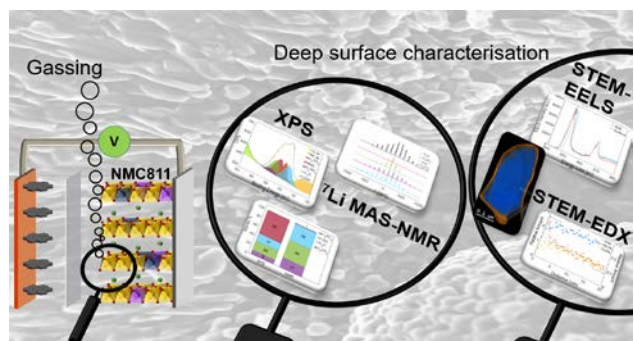
- (1) United Nations. Paris Declaration Electro-Mobility and Climate Change & Call to Action, 2015.
- (2) Myung, S.-T.; Maglia, F.; Park, K.-J.; Yoon, C. S.; Lamp, P.; Kim, S.-J.; Sun, Y.-K. Nickel-Rich Layered Cathode Materials for Automotive Lithium-Ion Batteries: Achievements and Perspectives. *ACS Energy Lett.* **2017**, *2* (1), 196–223. <https://doi.org/10.1021/acsenergylett.6b00594>.
- (3) Assat, G.; Tarascon, J.-M. Fundamental Understanding and Practical Challenges of Anionic Redox Activity in Li-Ion Batteries. *Nature Energy* **2018**, *3* (5), 373. <https://doi.org/10.1038/s41560-018-0097-0>.
- (4) Noh, H.-J.; Youn, S.; Yoon, C. S.; Sun, Y.-K. Comparison of the Structural and Electrochemical Properties of Layered Li[Ni_xCoyMnz]O₂ (x = 1/3, 0.5, 0.6, 0.7, 0.8 and 0.85) Cathode Material for Lithium-Ion Batteries. *Journal of Power Sources* **2013**, *233*, 121–130. <https://doi.org/10.1016/j.jpowsour.2013.01.063>.
- (5) Zhang, S.; Ma, J.; Hu, Z.; Cui, G.; Chen, L. Identifying and Addressing Critical Challenges of High-Voltage Layered Ternary Oxide Cathode Materials. *Chem. Mater.* **2019**, *31*, 33.
- (6) Murdock, B. E.; Toghill, K. E.; Tapia-Ruiz, N. A Perspective on the Sustainability of Cathode Materials Used in Lithium-Ion Batteries. *Advanced Energy Materials* **2021**, *11* (39), 2102028. <https://doi.org/10.1002/aenm.202102028>.
- (7) Jung, R.; Metzger, M.; Maglia, F.; Stinner, C.; Gasteiger, H. A. Oxygen Release and Its Effect on the Cycling Stability of LiNi_xMn_yCo_zO₂ (NMC) Cathode Materials for Li-Ion Batteries. *Journal of The Electrochemical Society* **2017**, *164* (7), A1361–A1377. <https://doi.org/10.1149/2.0021707jes>.
- (8) Gao, H.; Cai, J.; Xu, G.-L.; Li, L.; Ren, Y.; Meng, X.; Amine, K.; Chen, Z. Surface Modification for Suppressing Interfacial Parasitic Reactions of a Nickel-Rich Lithium-Ion Cathode. *Chem. Mater.* **2019**, *31* (8), 2723–2730. <https://doi.org/10.1021/acs.chemmater.8b04200>.

- (9) Sicklinger, J.; Metzger, M.; Beyer, H.; Pritzl, D.; Gasteiger, H. A. Ambient Storage Derived Surface Contamination of NCM811 and NCM111: Performance Implications and Mitigation Strategies. *J. Electrochem. Soc.* **2019**, *166* (12), A2322–A2335. <https://doi.org/10.1149/2.0011912jes>.
- (10) Renfrew, S. E.; McCloskey, B. D. Residual Lithium Carbonate Predominantly Accounts for First Cycle CO₂ and CO Outgassing of Li-Stoichiometric and Li-Rich Layered Transition-Metal Oxides. *Journal of the American Chemical Society* **2017**, *139* (49), 17853–17860. <https://doi.org/10.1021/jacs.7b08461>.
- (11) Zhu, J.; Sharifi-Asl, S.; Garcia, J. C.; Iddir, H. H.; Croy, J. R.; Shahbazian-Yassar, R.; Chen, G. Atomic-Level Understanding of Surface Reconstruction Based on Li[Ni_xMn_yCo_{1-x-y}]O₂ Single-Crystal Studies. *ACS Appl. Energy Mater.* **2020**, *3* (5), 4799–4811. <https://doi.org/10.1021/acsaem.0c00411>.
- (12) Han, B.; Key, B.; Lapidus, S. H.; Garcia, J. C.; Iddir, H.; Vaughey, J. T.; Dogan, F. From Coating to Dopant: How the Transition Metal Composition Affects Alumina Coatings on Ni-Rich Cathodes. *ACS Applied Materials & Interfaces* **2017**, *9* (47), 41291–41302. <https://doi.org/10.1021/acsami.7b13597>.
- (13) Nomura, Y.; Yamamoto, K.; Hirayama, T.; Ohkawa, M.; Igaki, E.; Hojo, N.; Saitoh, K. Quantitative *Operando* Visualization of Electrochemical Reactions and Li Ions in All-Solid-State Batteries by STEM-EELS with Hyperspectral Image Analyses. *Nano Lett.* **2018**, *18* (9), 5892–5898. <https://doi.org/10.1021/acs.nanolett.8b02587>.
- (14) Gu, M.; Belharouak, I.; Genc, A.; Wang, Z.; Wang, D.; Amine, K.; Gao, F.; Zhou, G.; Thevuthasan, S.; Baer, D. R.; Zhang, J.-G.; Browning, N. D.; Liu, J.; Wang, C. Conflicting Roles of Nickel in Controlling Cathode Performance in Lithium Ion Batteries. *Nano Lett.* **2012**, *6*.
- (15) Shukla, A. K.; Ramasse, Q. M.; Ophus, C.; Duncan, H.; Hage, F.; Chen, G. Unravelling Structural Ambiguities in Lithium- and Manganese-Rich Transition Metal Oxides. *Nature Communications* **2015**, *6* (1), 8711. <https://doi.org/10.1038/ncomms9711>.
- (16) Yan, P.; Zheng, J.; Zheng, J.; Wang, Z.; Teng, G.; Kuppam, S.; Xiao, J.; Chen, G.; Pan, F.; Zhang, J.-G.; Wang, C.-M. Ni and Co Segregations on Selective Surface Facets and Rational Design of Layered Lithium Transition-Metal Oxide Cathodes. *Advanced Energy Materials* **2016**, *6* (9), 1502455. <https://doi.org/10.1002/aenm.201502455>.
- (17) Sun, Y.-K.; Myung, S.-T.; Park, B.-C.; Prakash, J.; Belharouak, I.; Amine, K. High-Energy Cathode Material for Long-Life and Safe Lithium Batteries. *Nature Mater* **2009**, *8* (4), 320–324. <https://doi.org/10.1038/nmat2418>.
- (18) Ramakrishnan, S.; Park, B.; Wu, J.; Yang, W.; McCloskey, B. D. Extended Interfacial Stability Through Simple Acid Rinsing in a Li-Rich Oxide Cathode Material. October 16, 2019. <https://doi.org/10.26434/chemrxiv.9962471.v1>.
- (19) Doo, S. W.; Lee, S.; Kim, H.; Choi, J. H.; Lee, K. T. Hydrophobic Ni-Rich Layered Oxides as Cathode Materials for Lithium-Ion Batteries. *ACS Appl. Energy Mater.* **2019**, acsaem.9b00786. <https://doi.org/10.1021/acsaem.9b00786>.

- (20) Jung, R.; Morasch, R.; Karayaylali, P.; Phillips, K.; Maglia, F.; Stinner, C.; Shao-Horn, Y.; Gasteiger, H. A. Effect of Ambient Storage on the Degradation of Ni-Rich Positive Electrode Materials (NMC811) for Li-Ion Batteries. *Journal of The Electrochemical Society* **2018**, *165* (2), A132–A141. <https://doi.org/10.1149/2.0401802jes>.
- (21) Lee, W.; Lee, S.; Lee, E.; Choi, M.; Thangavel, R.; Lee, Y.; Yoon, W.-S. Destabilization of the Surface Structure of Ni-Rich Layered Materials by Water-Washing Process. *Energy Storage Materials* **2022**, *44*, 441–451. <https://doi.org/10.1016/j.ensm.2021.11.006>.
- (22) Busà, C.; Belekoukia, M.; Loveridge, M. J. The Effects of Ambient Storage Conditions on the Structural and Electrochemical Properties of NMC-811 Cathodes for Li-Ion Batteries. *Electrochimica Acta* **2021**, *366*, 137358. <https://doi.org/10.1016/j.electacta.2020.137358>.
- (23) Wood, M.; Li, J.; Ruther, R. E.; Du, Z.; Self, E. C.; Meyer, H. M.; Daniel, C.; Belharouak, I.; Wood, D. L. Chemical Stability and Long-Term Cell Performance of Low-Cobalt, Ni-Rich Cathodes Prepared by Aqueous Processing for High-Energy Li-Ion Batteries. *Energy Storage Materials* **2020**, *24*, 188–197. <https://doi.org/10.1016/j.ensm.2019.08.020>.
- (24) Lucas, G.; Burdet, P.; Cantoni, M.; Hébert, C. Multivariate Statistical Analysis as a Tool for the Segmentation of 3D Spectral Data. *Micron* **2013**, *52–53*, 49–56. <https://doi.org/10.1016/j.micron.2013.08.005>.
- (25) Dupré, N.; Martin, J.-F.; Guyomard, D.; Yamada, A.; Kanno, R. Detection of Surface Layers Using ^7Li MAS NMR. *Journal of Materials Chemistry* **2008**, *18* (36), 4266. <https://doi.org/10.1039/b807778a>.
- (26) Liu, H.; Bugnet, M.; Tessaro, M. Z.; Harris, K. J.; Dunham, M. J. R.; Jiang, M.; Goward, G. R.; Botton, G. A. Spatially Resolved Surface Valence Gradient and Structural Transformation of Lithium Transition Metal Oxides in Lithium-Ion Batteries. *Phys. Chem. Chem. Phys.* **2016**, *18* (42), 29064–29075. <https://doi.org/10.1039/C6CP05262B>.
- (27) Dixit, M.; Markovsky, B.; Schipper, F.; Aurbach, D.; Major, D. T. Origin of Structural Degradation During Cycling and Low Thermal Stability of Ni-Rich Layered Transition Metal-Based Electrode Materials. *J. Phys. Chem. C* **2017**, *121* (41), 22628–22636. <https://doi.org/10.1021/acs.jpcc.7b06122>.
- (28) Ménétrier, M.; Vaysse, C.; Croguennec, L.; Delmas, C.; Jordy, C.; Bonhomme, F.; Biensan, P. ^7Li and ^1H MAS NMR Observation of Interphase Layers on Lithium Nickel Oxide Based Positive Electrodes of Lithium-Ion Batteries. *Electrochem. Solid-State Lett.* **2004**, *7* (6), A140. <https://doi.org/10.1149/1.1697905>.
- (29) Grissa, R.; Fernandez, V.; Fairley, N.; Hamon, J.; Stephant, N.; Rolland, J.; Bouchet, R.; Lecuyer, M.; Deschamps, M.; Guyomard, D.; Moreau, P. XPS and SEM-EDX Study of Electrolyte Nature Effect on Li Electrode in Lithium Metal Batteries. *ACS Appl. Energy Mater.* **2018**, *1* (10), 5694–5702. <https://doi.org/10.1021/acs.aem.8b01256>.
- (30) C.D. Wagner; A.V. Naumkin; A. Kraut-Vass; J.W. Allison; C.J. Powell; J.R.Jr. Rumble. NIST Standard Reference Database 20, Version 3.4.

- (31) Köcher, S. S.; Schleker, P. P. M.; Graf, M. F.; Eichel, R.-A.; Reuter, K.; Granwehr, J.; Scheurer, Ch. Chemical Shift Reference Scale for Li Solid State NMR Derived by First-Principles DFT Calculations. *Journal of Magnetic Resonance* **2018**, 297, 33–41. <https://doi.org/10.1016/j.jmr.2018.10.003>.
- (32) Cuisinier, M.; Martin, J.-F.; Moreau, P.; Epicier, T.; Kanno, R.; Guyomard, D.; Dupré, N. Quantitative MAS NMR Characterization of the $\text{LiMn}_{1/2}\text{Ni}_{1/2}\text{O}_2$ Electrode/Electrolyte Interphase. *Solid State Nuclear Magnetic Resonance* **2012**, 42, 51–61. <https://doi.org/10.1016/j.ssnmr.2011.09.001>.
- (33) Cho, D.-H.; Jo, C.-H.; Cho, W.; Kim, Y.-J.; Yashiro, H.; Sun, Y.-K.; Myung, S.-T. Effect of Residual Lithium Compounds on Layer Ni-Rich $\text{Li}[\text{Ni}_{0.7}\text{Mn}_{0.3}]\text{O}_2$. *J. Electrochem. Soc.* **2014**, 161 (6), A920. <https://doi.org/10.1149/2.042406jes>.
- (34) Shizuka, K.; Kiyohara, C.; Shima, K.; Takeda, Y. Effect of CO_2 on Layered $\text{Li}_{1+z}\text{Ni}_{1-x-y}\text{Co}_x\text{Mn}_y\text{O}_2$ (M=Al, Mn) Cathode Materials for Lithium Ion Batteries. *Journal of Power Sources* **2007**, 166 (1), 233–238. <https://doi.org/10.1016/j.jpowsour.2007.01.013>.
- (35) Liu, W.; Oh, P.; Liu, X.; Lee, M.-J.; Cho, W.; Chae, S.; Kim, Y.; Cho, J. Nickel-Rich Layered Lithium Transition-Metal Oxide for High-Energy Lithium-Ion Batteries. *Angewandte Chemie International Edition* **2015**, 54 (15), 4440–4457. <https://doi.org/10.1002/anie.201409262>.
- (36) Shurtz, R. C.; Hewson, J. C. Review—Materials Science Predictions of Thermal Runaway in Layered Metal-Oxide Cathodes: A Review of Thermodynamics. *J. Electrochem. Soc.* **2020**, 167 (9), 090543. <https://doi.org/10.1149/1945-7111/ab8fd9>.
- (37) Wang, M.; Navrotsky, A. LiMO_2 (M=Mn, Fe, and Co): Energetics, Polymorphism and Phase Transformation. *Journal of Solid State Chemistry* **2005**, 178 (4), 1230–1240. <https://doi.org/10.1016/j.jssc.2005.01.028>.
- (38) Busà, C.; Belekoukia, M.; Loveridge, M. J. The Effects of Ambient Storage Conditions on the Structural and Electrochemical Properties of NMC-811 Cathodes for Li-Ion Batteries. *Electrochimica Acta* **2021**, 366, 137358. <https://doi.org/10.1016/j.electacta.2020.137358>.

TOC



For Table of Contents Only